Near-Infrared Light-Triggered "On/Off" Motion of Polymer Multilayer Rockets

Zhiguang Wu,[†] Xiankun Lin,[†] Yingjie Wu, Tieyan Si,* Jianmin Sun, and Qiang He*

State Key Laboratory of Robotics and System (HIT), Academy of Fundamental and Interdisciplinary Sciences, Harbin Institute of Technology, Harbin 150080, China.
[†]Z. Wu and X. Lin contributed equally to this work.

ABSTRACT We describe an approach to modulating the on-demand motion of catalytic polymer-based microengines *via* near-infrared (NIR) laser irradiation. The polymer multilayer motor was fabricated by the template-assisted layer-by-layer assembly and subsequently deposition of platinum nanoparticles inside and a thin gold shell outside. Then a mixed monolayer of a tumor-targeted peptide and an antifouling poly(ethylene glycol) was functionalized on the gold shell. The microengines remain motionless at the critical peroxide concentration (0.1%, v/v); however, NIR illumination on the engines leads to a photothermal effect and thus rapidly triggers the motion of the catalytic engines. Computational modeling explains the photothermal effect and gives the temperature profile accordingly. Also, the photothermal effect can alone activate the motion of the engines in the absence of the peroxide fuel, implying that it may eliminate the use of toxic fuel in the future. The targeted recognition ability and subsequently killing of cancer cells by the photothermal effect under the higher power of a NIR laser were illustrated. Our results pave the way to apply self-propelled synthetic engines in biomedical fields.

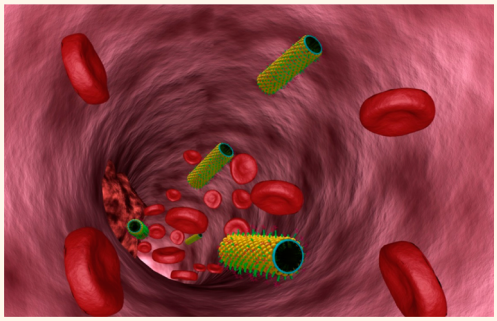

KEYWORDS: layer-by-layer · autonomous motion · synthetic motor · recognition · photothermal effect

Controlled motion and transport of small objects at the micro- and nanoscale have displayed impressive potential applications in diverse fields such as drug delivery,[1,2] detection and isolation of biological targets,[3−5] development of lab-on-a-chip devices,[6,7] and dynamic self-assembly.[8−14] In nature living organisms leave or approach a targeted site through biological behaviors such as chemotaxis, phototaxis, and aerotaxis.[15−17] Inspired by these biological behaviors of organisms, diverse synthetic motors such as microjet engines,[18,19] bimetal nanorods,[20−22] helix swimmers,[23−25] Janus particles,[26−28] and metal- or polymer-based microtubes[29−31] have been developed in the past decade, and more information on the synthesis and mechanism can be found in recent reports.[32−40] Moreover, these pioneering studies have demonstrated that the motion of the synthetic motors can be controlled by a magnetic field,[41,42] light,[43,44] heat,[45−47] and even the concentration gradient of fuel.[48,49] Concerning real biomedical and nanotechnological applications, however, remote interventions such as an external physical trigger are usually required to effectively control synthetic motors including the states (launch and stop) and direction of movement as well as the position and time that the motors work. The use of a physical input can be turned on or off on-demand, and, hence, a higher control over object motion can be achieved in a wide range of environments.

Recently light has exhibited the outstanding advantage of the control of motors since it is one of the most powerful and versatile physical triggers. For instance, the motion of colloidal motors was switched "on/off" by ultraviolet (UV) light *via* a self-diffusiophoretic mechanism,[50] and visible light triggered the launch of rolled-up catalytic microtubes.[51] However, UV light is strongly invasive to living organisms, while it is difficult for visible light to penetrate tissues. In contrast, light in the near-infrared (NIR) region is of special interest in the context of biomedical applications because body tissue has

* Address correspondence to qianghe@hit.edu.cn; tieyansi@hit.edu.cn.

Received for review March 11, 2014 and accepted May 7, 2014.

Published online May 07, 2014
10.1021/nn501407r

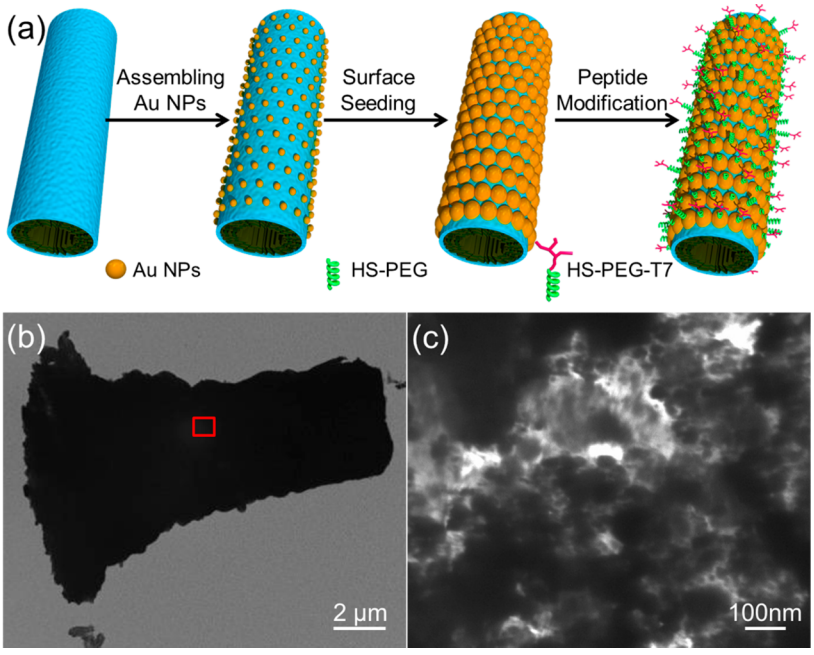

Figure 1. (a) Scheme of the fabrication process of the PtNP-modified polyelectrolyte multilayer microengines coated with a thin AuNS and a tumor-targeted peptide: (i) assembling gold nanoparticles on the outer surface of the tubes, (ii) growth of gold nanoparticles, and (iii) immobilization of the mixed thiol-PEG and thiol-peptide monolayer. (b) TEM image of a T7 AuNS $(PAH/PSS)_{20}$ PtNP microengine. (c) Enlarged image of the indicated region with a red frame in (b).

the highest transmissivity in this region (the so-called biological window). The plasmon resonance of gold nanostructures such as gold nanoparticles (Au NPs), gold nanorods, and gold nanoshells (AuNSs) can conveniently be tuned from the visible region into the NIR by changing their size and shape. As a result, they can convert the absorbed photons into thermal energy, which makes them attractive as photothermal agents for disease imaging and therapy.[52] Also, gold possesses a well-established gold−thiol bond chemistry that allows easy functionalization of the gold surface with a wide variety of ligands and targeting moieties.

Herein, we demonstrate how the NIR-triggered "on/off" motion of platinum nanoparticle (PtNP)-modified polymer multilayer micromotors coated with a thin AuNS and a tumor-targeted peptide can be achieved at a critical concentration of a peroxide fuel (0.1%, v/v). In previous studies, it has been found that at lower peroxide concentrations the generation of microbubbles is significantly reduced, but can be enhanced with the increase of the solution temperature.[46] This implies that the motility of the catalytic microengines can be modulated by a small change in the localized temperature. In this paper, upon NIR irradiation at the plasmon resonance of a AuNS, electromagnetic energy is absorbed and dissipated as heat into the surrounding media. The increase in temperature inside the microengines thus results in the accelerated kinetics of the catalytic chemical process, increased rates of mass transport, and enhanced instability of oxygen bubbles on the catalyst. Thus, the generated thermal energy under NIR illumination can be used to rapidly trigger the motion of catalytic microengines. Also, we will illustrate that the photothermal effect can alone activate the on-demand motion of these microengines in the absence of the peroxide fuel. Finally, we will illustrate the ability of the microengines for targeted recongnition and subsequently killing of cancer cells by the photothermal effect under the higher power of a NIR laser.

RESULTS AND DISCUSSION

The fabrication process of the multifunctionalized microengines is schematically described in Figure 1a. The frameworks of 20 bilayers of poly(allylamine hyhrochloride) (PAH)/poly(styrenesulfonic acid) (PSS) were first assembled through a nanoporous template-assisted layer-by-layer (LbL) technique according to the previously reported method.[53,54] Then, poly(diallyldimethylammonium chloride) (PDADMAC)-stabilized PtNPs are assembled in the inner surface of the $(PSS/PAH)_{20}$ tubes as a catalyst layer. The PtNPs are able to catalytically decompose hydrogen peroxide to release water and oxygen. The oxygen bubbles could propel the movement of the microengine or nanorockets in certain conditions.[51,53] Also, citrate-stabilized AuNPs with negative charges were assembled on the outer surface of the tubes through electrostatic attraction. Upon the addition of NH_2OH and $HAuCl_4$, AuNPs on the tubes served as the seeds for the growth of AuNS by the hydroxylamine seeding procedure.[55] Finally, a binary mixed monolayer of thiol-modified poly(ethylene glycol) (HS-PEG2000) and thiol-modified peptide ($HS\text{-}CH_2COO\text{-}(CH_2CH_2O)_7$-HRPYIAH, T7) (1:9 molar ratio)

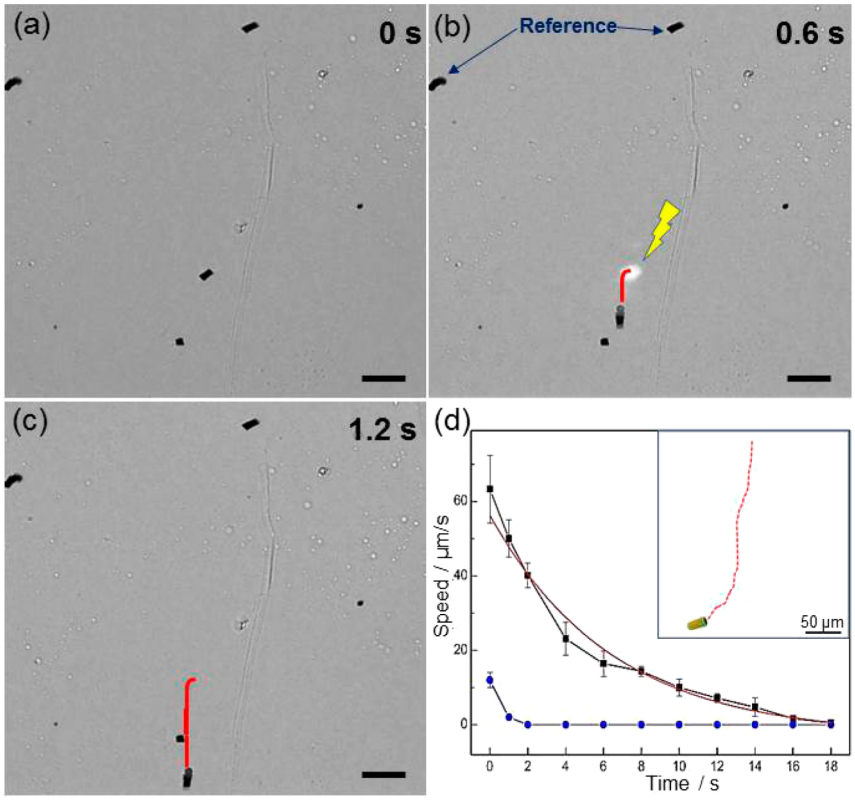

Figure 2. NIR-triggered launch of the T7 AuNS $(PAH/PSS)_{20}$ PtNPs microengine. (a, b, and c) Time-lapse images of the motion, which show the NIR-induced launch of a microengine in 0.1% (v/v) H_2O_2 solution. Scale bar = 20 μm. (d) Speed of the launched T7 AuNS $(PAH/PSS)_{20}$ PtNP microengine in 0.1% (v/v) H_2O_2 (black line) and in water (blue line) after the microengines were out of the laser spots. The smooth red line is fitted with an exponential decay. The inset is the tracking line of the motor after the irradiation of a NIR in 0.1% (v/v) H_2O_2.

was assembled onto the surface of the AuNS. Peptide T7 containing the HAIYPRH sequence has been shown to specifically bind to the human transferrin receptors (HTfR) and be 100-fold overexpressed on some tumor cells.[56,57] The use of MeO-PEG2000-SH is helpful to minimize the nonspecific binding of the engines on the tumor cells.

The transmission electron microscopy (TEM) image in Figure 1b shows the asymmetric conical structure of an as-assembled T7 AuNS $(PAH/PSS)_{20}$ tube like in our previous report. The length of the tube is approximately 10 μm, and the diameters of the two openings are approximately 5 and 7 μm, respectively. Interestingly, the enlarged image in Figure 1c reveals the higher surface roughness of the tube, which will possibly lead to a strong adsorption in the NIR region. The scanning electron microscope (SEM) image and the corresponding energy-dispersive X-ray (EDX) mapping in SI Figure 1 further verify the presence of gold on the microengines. The UV−vis spectrum in SI Figure 2 confirms the maximum adsorption of as-prepared T7 AuNS $(PAH/PSS)_{20}$ tubes at about 780 nm.

Figure 2a illustrates that no microbubbles were observed on T7 AuNS $(PAH/PSS)_{20}$ PtNP microengines, and thus the microengines remained immobile in hydrogen peroxide (H_2O_2) at a concentration of 0.1% (v/v). It should be noted that the catalytic decomposition rate of H_2O_2 is too low to power self-propulsion of the engines at this concentration level. In order to better explore this, we employed a centimeter-sized glass slide coated with $(PAH/PSS)_{20}$PtNPs for the optical investigation of the formation of oxygen bubbles at 0.1% (v/v) H_2O_2. SI Figure 3 shows that the oxygen bubbles still slowly formed, but most of them did not detach from the surface. As a result, the formation of oxygen bubbles decreases the diffusion of the reactant (H_2O_2) onto the catalyst (PtNPs) and further limits the occurrence of a catalytic decomposition reaction. When the solution temperature was increased to 70 °C, however, the formed bubbles rapidly detached from the surface and then more bubbles were continually produced. Similarly, upon projecting a focused NIR laser beam at 780 nm with a power of 3 mW/μm^2 (a size of about 50 μm^2) on the T7 AuNS

$(PAH/PSS)_{20}$ PtNP engine, a tail of microbubbles could be immediately observed on the rear of the engine and the engine began to move at the same time. The time-lapse images in Figure 2, captured from SI Video 1, display the launch of a T7 AuNS $(PAH/PSS)_{20}$ PtNP microengine under the irradiation of a focused NIR laser in 0.1% (v/v) H_2O_2. As a comparison, other unirradiated engines are used as the references, marked

by the arrows. It can be seen that the NIR-activated microengine accelerated within 0.6 s and then reached a maximum speed of about 62 μm/s compared to the reference microengines. Then the speed of the microengine gradually decreased from 62 μm/s to 0 μm/s in 20 s. According to the trajectory of the micromotor after leaving the laser spot as shown in the inset image of Figure 2d and SI Video 1, one could also see that the movement directions are not random, confirming that the movement is not Brownian. The microengine traveled a distance of more than 250 μm during this process. It is important to note that once a NIR-activated microengine starts to move, it will leave the focused area of the NIR laser. Like the above-mentioned mechanism, the sharp increase in temperature surrounding the microengines due to NIR irradiation rapidly induces higher rates of catalytic decomposition of H_2O_2 and mass transport of H_2O_2 and O_2, producing more oxygen bubbles and stronger propulsion force accordingly. Also, the higher temperature is favorable to the rapid release of the generated bubbles. Consequently, the higher frequency of bubble release leads to a higher speed of motion. Therefore, it is clear that exposure of a microengine to the focused NIR laser could induce a fast thermally modulated motion with a sharp increase in velocity. Furthermore, the residual heat could still maintain a higher temperature so that the catalytic decomposition of peroxide fuel continues to occur even though the engine has left the laser spot. This could be confirmed from the release of bubbles as shown in SI Video 1. Similar phenomena were also reported for large rolled-up microengines.[43]

The black line in Figure 2d shows the relationship of the speed of the microengines with time after they leave the focused region of the NIR laser. It can be seen that the speed deceleration of the microengines fits well with an exponential decay curve to some extent (red line in Figure 2d), $V = V_0\, e^{-bt}$, where V is the speed, V_0 is the initial speed, b is the decay rate, and t is the time. According to the heat transfer equation, the temperature of micromotors after they leave the focused region of NIR laser also shows an exponential decay (see the theoretical simulation in the Experimental Section). Since temperature is the most influential factor for changing the propelling force on the engine, the coincidence between the speed deceleration and the temperature decay follows a deep physical principal. This also reflects the changes of kinetics of the catalytic decomposition of peroxide fuel and the rates of mass transport. In a control experiment, a focused NIR laser with a power of 3 mW/μm^2 was used to illuminate a micromotor in pure water.

The blue line in Figure 2d shows that the micromotor could also be launched and instantly accelerated to the maximum speed of about 18 μm/s, but it fully stopped in 1.5 s (also see SI Figure 4 and SI Video 2). The change of speed of the micromotors under NIR irradiation in pure water or 0.1% (v/v) H_2O_2 has a similar tendency, revealing that the motion of the micromotors is directly related to the Soret effect or thermophoresis.[44] Such a unidirectional motion should derive from a thermal gradient due to the photothermal effect of the micromotors with an asymmetric shape. Comparing the speed of the micromotors in 0.1% H_2O_2 (black line) (v/v) and pure water (red line) in Figure 2d, it can be seen that the thermophoresis directly contributes a small fraction to the sharp increase in speed of the micromotor in 0.1% (v/v) H_2O_2 at the current power of the NIR laser.

We theoretically computed the photothermal effect of the micromotor under NIR irradiation. Briefly, the NIR laser strongly enhanced the motion of electrons in the Au film under the plasmon resonance, and thus the Au film heats up rapidly in a few picoseconds. The heat diffusion equation has widely been used to study the thermoplasmonics modeling of metallic particles.[57] Figure 3 shows the temperature gradient profile around the micromotors that is obtained by solving the heat diffusion equation. The details of the mathematical illustration can be found in the Experimental Section. Since the engine is modeled as a Au film covering an asymmetric cylinder, the temperature is highly localized around the cylinder. The rapid decay of temperature at the interface between the Au film and water is due to the large difference in thermal conductivity between the gold crystal and liquid water. Figure 3b reveals that the temperature grows almost linearly with laser power at a fixed position inside and outside the engine. This linear behavior is actually in good agreement with other thermoplasmonics modeling of smaller particles.[58−60]

The T7/PEG2000-functionalized T7 AuNS $(PAH/PSS)_{20}$ PtNP micromotors can selectively bind to target cancer cells but cannot attach to normal human cells. The time-lapse images of Figure 4 along with the corresponding SI Video 3 display that a self-propelled T7 AuNS $(PAH/PSS)_{20}$ PtNP micromotor approaches red blood cells (RBCs) at a speed of 15 μm/s, but was unable to capture or pick up RBCs. It is noted that no RBCs were observed to nonspecifically bind to the micromotors during the experimental process. This is because the increased hydrophilicity, high surface mobility, and steric stabilization effect of the assembled poly(ethylene glycol) chains can effectively prevent the nonspecific recognition between the micromotors and cells. In contrast, the images in Figure 5a, b, and c, captured from SI Video 4, demonstrate that a motionless T7 AuNS $(PAH/PSS)_{20}$ PtNP micromotor was launched by applying a focused NIR laser beam with a power of 3 mW/μm^2 and then moved to the HeLa cell sheets at an average speed of 42 μm/s at 0.1% (v/v) H_2O_2. Once the engines bound to the target HeLa cells, detachment was not recorded for over 1 h. The speed of the T7 AuNS $(PAH/PSS)_{20}$ PtNPs

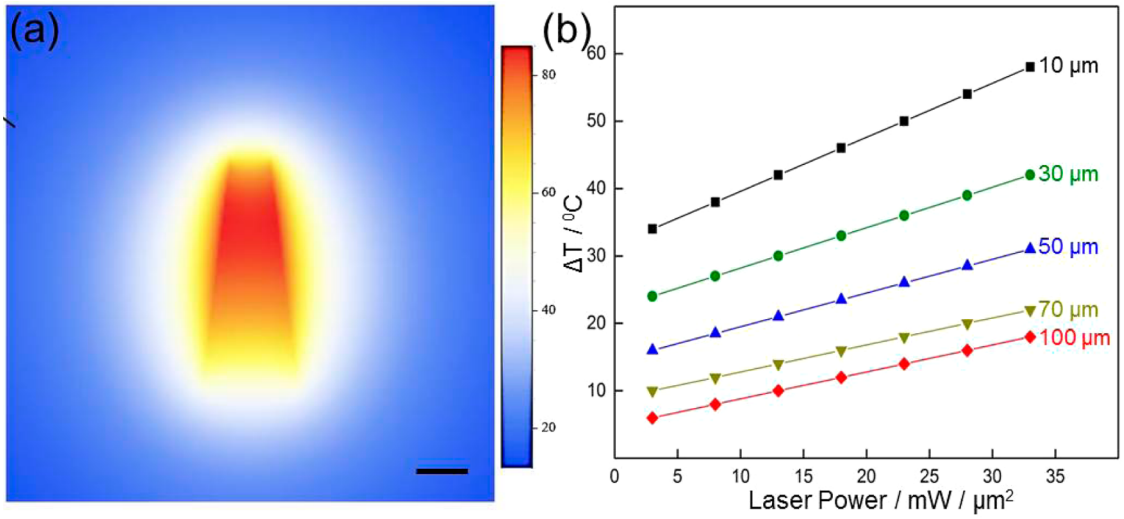

Figure 3. Theoretical simulation of the photothermal effect of a micromotor. (a) Elevated profile of temperature on the vertical cross section of the engine irradiated with a laser power of 3 mW/μm^2. The color bar shows the increase in temperature (°C). Scale bar = 5 μm. (b) Dependence of the NIR-induced temperature increase on both the laser power at a nearby position and the distance with respect to the center of T7 AuNS (PAH/PSS)$_{20}$ PtNP micromotors.

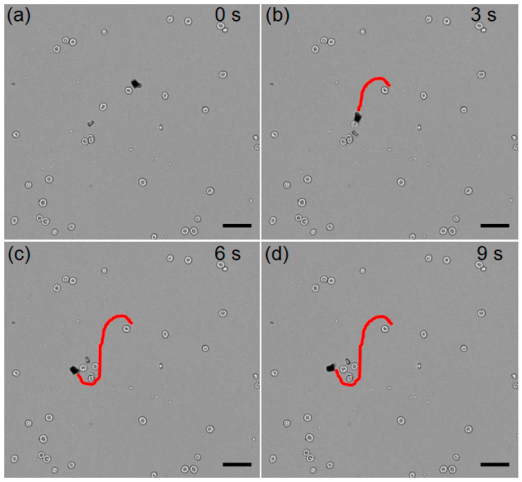

Figure 4. Time-lapse images of motion of a T7 AuNS-(PAH/PSS)$_{20}$ PtNP micromotor toward red blood cells in a 0.5% H_2O_2 solution. Scale bar = 20 μm.

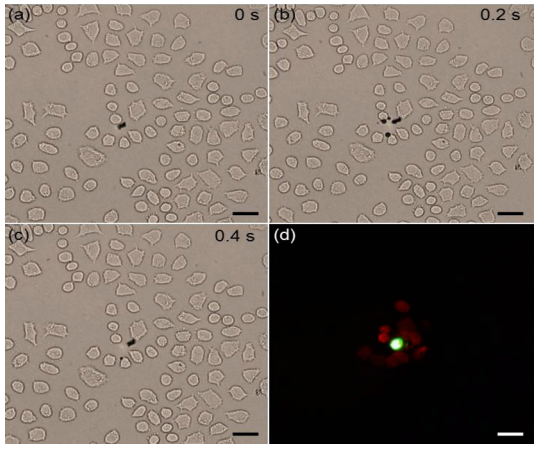

Figure 5. Targeted photothermal therapy of the T7 AuNS (PAH/PSS)$_{20}$ PtNP micromotor on the model HeLa cells. (a, b, and c) Time-lapse images of the NIR-triggered motion of the T7 AuNS (PAH/PSS)$_{20}$ PtNP micromotor toward HeLa cells in 0.1% (v/v) H_2O_2. (d) Corresponding fluorescence image of the engine radiated by the NIR laser with the power of 13 mW/μm^2 for 5 s. Scale bar = 20 μm.

micromotor is affected in a cell incubation environment containing 0.1% (v/v) H_2O_2 (*e.g.*, decreasing from 63 μm/s to 42 μm/s), but still preserves its high transport ability. Basically, these images and videos indicate that the as-assembled micromotors are capable of selectively binding to HeLa cancer cells though the T7 peptide modification and almost eliminate the nonspecific recognition of RBCs.

According to our simulation (Figure 3b), the increase in temperature caused by the photothermal effect of the Au NS is largely dependent on the output power of the used NIR laser. After the engine bound to the HeLa cell, the beam of the NIR laser was realigned to focus on the engine, and spontaneously the output power was improved at the power of 13 mW/μm^2 for 5 s. At that moment, the maximum temperature of the micromotor can reach approximately 59 °C, and the elevated temperature in a 70 μm radius around the engine is more than 10 °C (Figure 3b). This change in temperature is enough to induce the apoptosis of HeLa cells in this region. The fluorescence microscopy image in Figure 5d displays the red fluorescence of the nuclei of HeLa cells in roughly a 60 μm radius around the engine. The red fluorescence came from the preadded fluorescent dye, propidium iodide (PI). PI can penetrate into the nuclei after the breakage of cell membranes and has thus been widely employed to test cell apoptosis. As a result, the red fluorescence from the cell nuclei around the micromotor represents the distinct apoptotic feature of HeLa cells, indicating that as-assembled

T7 AuNS $(PAH/PSS)_{20}$ PtNP micromotors can also be used as a photothermal agent for a minimally invasive, selective treatment of cancer. Also, the radius of the apoptotic cell sheet around the NIR-irradiated micromotor roughly corresponds to our simulated range. Moreover, it is important to note that there is no red fluorescence in other areas, suggesting that 0.1% (v/v) H_2O_2 did not induce the apoptosis of cancer cells in our case.

CONCLUSION

We have demonstrated a new strategy for photothermally triggering the "on-demand" launch of gold shell-functionalized polymer multilayer micromotors using a NIR laser at the critical concentration of peroxide fuel. This process is based on the fact that NIR illumination of the micromotors causes a spontaneous photothermal effect and thus a locally sharp increase in temperature around the micromotors. Accordingly, the increase in temperature induces the accelerated kinetics of the catalytic decomposition, the increased rates of mass transport, and the enhanced release frequency of oxygen bubbles. These micromotors can be readily functionalized with targeting ligands for highly specific cancer recognition and subsequent photothermal cancer therapy. Therefore, our micromotors have integrated the features of a controllable launch promoted by a NIR laser, self-propulsion, dynamic target recognition of cancer cells, and photothermal therapy ability. Such multifunctionalized micromotors hold great promise for diverse future applications of synthetic nanomotors. More interestingly, we found that the photothermal effect can be used alone to activate the motion of micromotors in the absence of peroxide fuel, and more in-depth studies and theoretical simulations are ongoing in our laboratory.

EXPERIMENTAL SECTION

Fabrication of AuNS $(PAH/PSS)_{20}$ PtNP Micromotors. The AuNS $(PAH/PSS)_{20}$ PtNP micromotors were fabricated through a modified template-assisted layer-by-layer assembly.[53] The citrate-stabilized gold nanoparticles and PDADMAC-stabilized Pt nanoparticles were prepared according to the previous methods.[61,62] Polycarbonate membranes with a pore diameter of 5 μm (catalog no. 7060-2513, Whatman, U.K.) were used as the templates. Briefly, the template was alternatively immersed into PAH (1 mg/mL in 0.5 M NaCl) and PSS (1 mg/mL in 0.5 M NaCl) solutions for 30 min to form one (PAH/PSS) bilayer. After 20 bilayers of PAH/PSS were deposited into the template, the PtNPs were assembled into the template as the innermost layer. The materials adsorbed on the top and bottom surfaces of the template were removed by polishing and wiping the surfaces of the template with wet cotton swabs. The $(PAH/PSS)_{20}$ PtNP micromotors can be obtained by dissolving the templates in CH_2Cl_2.

The $(PAH/PSS)_{20}$ PtNP micromotors were incubated in a solution of citrate-stabilized AuNPs for 30 min. The method of hydroxylamine seeding was used to form the gold nanoshell on the outer surface of the AuNP $(PAH/PSS)_{20}$ PtNP micromotors.[55] The AuNP $(PAH/PSS)_{20}$ PtNP engines were released in a 1.5 mL aqueous solution including 50 μL of NH_2OH and 0.1% (w/v) $HAuCl_4$, and the mixture was stirred slightly for about 10 min to allowed the reduction of $HAuCl_4$ to grow shells on the outer surface of the micromotors. The AuNS $(PAH/PSS)_{20}$ PtNP micromotors were collected by applying centrifugation at 4000*g* for 3 min and stored at 4 °C.

Target T7 Peptide Modification of AuNS $(PAH/PSS)_{20}$ PtNP Micromotors. The outer surface of Au nanoshells of the micromotors was modified by the target T7 peptide to get the T7AuNS $(PAH/PSS)_{20}$ PtNP micromotors. The AuNS $(PAH/PSS)_{20}$ PtNP micromotors were incubated with a binary mixture of 2 mM MeO-PEG2000-SH and 0.2 mM T7 peptide (molar ratio, 1:9) in 80% (v/v) ethanol overnight. After washing with ultrapure water, the obtained T7 AuNS $(PAH/PSS)_{20}$ PtNP micromotors were stored at 4 °C.

Cell Experiment. Healthy red blood cells were obtained from the hospital of the Harbin Institute of Technology and added with ethylenediamine tetraacetate (EDTA) to prevent coagulation. The apoptosis of the HeLa cells induced by T7 AuNS $(PAH/PSS)_{20}$ PtNP micromotors under the treatment of a NIR laser was determined by the modified PI staining method.[53] A 5 μL amount of PI was added to 20 mL of the cell culture prior to the NIR treatment, and the apoptosis of the HeLa cells was confirmed by fluorescent imaging.

Characterization. Transmission electron microscopy analysis was performed on a Tecnai G2 F30 microscope operated at 120 kV. The samples were prepared on a carbon-coated copper grid. An Olympus BX53F optical microscope, coupled with a 20× objective and relative software, was used to capture videos.

Theoretical Modeling. Barrat *et al.* recently simulated the photothermal effect of gold nanoparticles with diameters of 500 nm based on the arranged 494 gold atoms on a face of the nanoparticles.[56] Their result shows that the elevated temperature should be highly localized around the nanoparticles. The temperature profile of an illuminated engine should be quite similar to that of a spherical particle. Both the width and length of our engines are larger than the wavelength of the used laser, and the electromagnetic wave is oscillating as a standing wave along the tubular Au film. The film thickness is much smaller than both the length and width of the micromotors, and we can take it as a two-dimensional surface to mathematically model the temperature.

Since the thermal conductivity of gold (318 W/mK) is much higher than that of water (0.6 W/mK) and air (0.025 W/mK), there is a sudden temperature drop at the interface between the engines and water. The temperature at the interface can be estimated by the following equation.[63]

$$T(r) = \frac{T_{\text{tube}}\sqrt{\rho_{\text{Au}}C_{\text{Au}}k_{\text{Au}}} + T_{\omega}\sqrt{\rho_{\text{w}}C_{\omega}k_{\text{w}}}}{\sqrt{\rho_{\text{Au}}C_{\text{Au}}k_{\text{Au}}} + \sqrt{\rho_{\text{w}}C_{\omega}k_{\text{w}}}} \quad (1)$$

where C is the specific heat, k is thermal conductivity, and ρ is mass density.

The melting point of crystalline Au is 1064.18 °C. If the temperature of the micromotor is higher than the melting point, the gold film will melt into a liquid. If the particle has a temperature of 1000 °C in the Au film, the temperature of the water should thus be about 600 °C at the interface, and then it decays following $T(r) = A + B/r$.[60] The quantitative profile of temperature of an optically stimulated micromotor obeys the usual heat transfer equation:[58]

$$\rho(r)\, c(r)\, \frac{\partial T(r)}{\partial T} = \nabla k(r)\, \nabla T(r) + Q(r, t) \quad (2)$$

where $T(r, t)$ is temperature as a function of coordinate and time, $\rho(r)$ is the mass density, $c(r)$ is the specific heat, $k(r)$ is thermal conductivity, and $Q(r, t)$ is the energy source stimulated by the laser; $Q(r,t) = \langle j(r,t)\, E(r,t)\rangle$. The heat generation from a tubular particle is slightly different from that of a spherical particle,

$$Q(r, t) = \frac{\omega}{8\pi} E^2 \left|\frac{2\varepsilon_0}{\varepsilon_0 + \varepsilon_{\text{NP}}}\right|^2 \text{Im}\ \varepsilon_{\text{NP}} \quad (3)$$

The power density absorbed by a material is $P = \omega\varepsilon|E|^2$. The temperature reaches a stable distribution in a few microseconds. For a steady distribution of temperature in an infinitely large tank, the heat transfer equation obeys $\partial T(r, t)/\partial T = 0$. The heat transfer equation reduced to a Poisson equation, $\nabla k(r)\ \nabla T(r) = Q(r, t) = q\sum_i \delta(r - r_i)$. According to Green function theory, $\nabla k(r)\ \nabla T(r) = Q(r, t) = q\sum_i \delta(r - r_i)$, a typical solution has the following distribution:

$$\Delta T(r) = \frac{V_{np}Q}{4\pi k(r - r_0)} \tag{4}$$

This solution fulfills the Green function equation, $\Delta T(r) = V_{np}QGr_i$; here $G(r) = 1/[4\pi k(r - r_i)]$ is called the Green function. The maximal temperature increase is proportional to the light intensity:

$$\Delta T_{max} = CV_{tube}\left|\frac{2\varepsilon_0}{\varepsilon_0 + \varepsilon_{NP}}\right|^2 I_0/k_0 \tag{5}$$

The temperature profile $\Delta T(r)$ is the contribution of only one particle. For an ensemble of many particles distributed on a complex geometry, the final temperature profile is given by $T = \sum_i G(r_i)Q_i$. Note that the engine in our experiment is an asymmetric cylinder, as shown in Figure 1b. We take a pyramid cylinder as an approximation of the engine. The thick Au film is roughly thought of as a continuous film due to its high density of gold particles. The sum of all Green functions is the integral of the asymmetric cylinder surface:

$$G(r_i, z) = \int_0^{2\pi} d\phi \int_0^{c} d\theta \frac{1}{4\pi k_0 \sqrt{r^2\left(1 + 4\frac{\alpha\sin[A]}{\sin[\theta + A]}\tan^2\left[\frac{\phi}{2}\right]\cos^2[\theta]\right) + \left(5 - 4\tan^2\left[\frac{\theta}{2}\right]\cos^2[\theta]\right)\frac{\alpha^2\sin^2[A]}{\sin^2[\theta + A]}}} \tag{6}$$

where $\tan[A] = h/(a - b)$; $\tan[c] = h - b$. The pyramid cylinder becomes a standard cylinder when $a = b$. Then the green function above has a simpler formulation:

$$G(r, z, \phi) = \frac{1}{4\pi k\sqrt{r^2 + {r_0}^2 - 2r_0 r\cos[\phi] + (z_0 + z)^2}} \tag{7}$$

The temperature profile has rotational symmetry around the central axis of the cylinder ($x = 0$; $y = 0$; z). We check the temperature profile only on the cross section that cuts the cylinder into two semispherical cylinders (Figure 3a). The continuous temperature profile on this cross section around the micromotor is given by $T(r) = \int dz \int d\phi\ G(r)Q$. First we integrate the angle φ,

$$G(r, z) = \int d\phi\ G(r, z, \phi) = \int_0^2 d\phi \frac{1}{4\pi k\sqrt{r^2 + {r_0}^2 - 2r_0 r\cos[\phi] + (z_0 + z)^2}} \tag{8}$$

Its output is an elliptic function over distance,

$$G(r, z) = \frac{K\left[-\frac{4r_0 r}{(r - r_0)^2 + z^2 + 2zz_0 + {z_0}^2}\right]}{\sqrt{(r - r_0)^2 + z^2 + 2zz_0 + {z_0}^2}} \tag{9}$$

here $K[x]$ represents elliptic $K[x]$, the complete elliptic integral of the first kind. Integrating the Green function over the length direction leads to the equation of the temperature profile on the cross section,

$$T(r) = Q\int_0^h dz\ G(r, z) = Q\int_0^h dz \frac{K\left[-\frac{4r_0 r}{(r - r_0)^2 + z^2 + 2zz_0 + {z_0}^2}\right]}{\sqrt{(r - r_0)^2 + z^2 + 2zz_0 + {z_0}^2}} \tag{10}$$

The above solution is for a standard cylinder. For a pyramidal cylinder of Au film, we cut the pyramidal cylinder into many layers of short elementary cylinders and performed integration over the height to solve the heat transfer equation in MatLab. The maximal temperature is around the center of the narrow top, and the temperature of the wide base is lower than the top. The profile of the temperature becomes symmetric 8 μm away from the center axis of the micromotor. In the vicinity of the micromotor, the temperature profile is highly asymmetric. The highly localized temperature is consistent with other theoretical works.[57−60]

Conflict of Interest: The authors declare no competing financial interest.

Acknowledgment. We thank Prof. J. B. Li (ICCAS, Beijing) for support. This work was supported by the National Nature Science Foundation of China (91027045 and 21103034), New Century Excellent Talent Program (NCET-11-0800), and State Key Laboratory of Robotics and System (HIT).

Supporting Information Available: Additional images and videos. This material is available free of charge *via* the Internet at http://pubs.acs.org.

REFERENCES AND NOTES

1. Wang, J. *Nanomachines: Fundamentals and Applications*; Wiley-VCH: Weinheim, Germany, 2013.
2. Mallouk, T. E.; Sen, A. Powering Nanorobots. *Sci. Am.* **2009**, *300*, 72–77.
3. Mei, Y. F.; Solovev, A. A.; Sanchez, S.; Schmidt, O. G. Rolled-up Nanotech on Polymers: From Basic Perception to Self-Propelled Catalytic Microengines. *Chem. Soc. Rev.* **2011**, *40*, 2109–2119.
4. Wang, W.; Duan, W.; Ahmed, S.; Mallouk, T. E.; Sen, A. Small Power: Autonomous Nano- and Micromotors Propelled by Self-Generated Gradients. *Nano Today* **2013**, *8*, 531–554.
5. Sanchez, S.; Pumera, M. Nanorobots: The Ultimate Wireless Self-propelled Sensing and Actuating Devices. *Chem.—Asian J.* **2009**, *4*, 1402–1410.
6. Sanchez, S.; Solovev, A. A.; Harazim, S. M.; Schmidt, O. G. Microbots Swimming in the Flowing Streams of Microfluidic Channels. *J. Am. Chem. Soc.* **2011**, *133*, 701–703.
7. Gao, W.; Kagan, D.; Pak, O. S.; Clawson, C.; Campuzano, S.; Chuluun-Erdene, E.; Shipton, E.; Fullerton, E. E.; Zhang, L.; Lauga, E.; Wang, J. Cargo-Towing Fuel-Free Magnetic Nanomotors for Targeted Drug Delivery. *Small* **2012**, *8*, 460–467.
8. Gao, W.; Pei, A.; Feng, X.; Hennessy, C.; Wang, J. Organized Self-Assembly of Janus Micromotors with Hydrophobic Hemispheres. *J. Am. Chem. Soc.* **2013**, *135*, 998–1001.
9. Kuralay, F.; Sattayasamitsathit, S.; Gao, W.; Uygun, A.; Katzenberg, A.; Wang, J. Self-Propelled Carbohydrate-Sensitive Microtransporters with Built-in Boronic Acid Recognition for Isolating Sugars and Cells. *J. Am. Chem. Soc.* **2012**, *134*, 15217–15220.
10. Ismagilov, R. F.; Schwartz, A.; Bowden, N.; Whitesides, G. M. Autonomous Movement and Self-Assembly. *Angew. Chem., Int. Ed.* **2002**, *114*, 652–654.
11. Ishihara, S.; Wakayama, Y.; Hiroshiba, N.; Hill, J.; Ariga, K. Novel Concepts for Organic Syntheses Based on Interfaces and Molecular Machines. *Curr. Org. Synth.* **2012**, *9*, 428–438.
12. Panman, M. R.; Bodis, P.; Shaw, D. J.; Bakker, B. H.; Newton, A. C.; Kay, E. R.; Brouwer, A. M.; Buma, W. J.; Leigh, D. A.; Woutersen, S. Operation Mechanism of a Molecular Machine Revealed Using Time Resolved Vibrational Spectroscopy. *Science* **2010**, *328*, 1255–1258.
13. Tottori, S.; Zhang, L.; Qiu, F.; Krawczyk, K. K.; Franco-Obregon, A.; Nelson, B. J. Magnetic Helical Micromachines: Fabrication, Controlled Swimming, and Cargo Transport. *Adv. Mater.* **2012**, *24*, 811–816.
14. Ozin, G. A.; Manners, I.; Fournier-Bidoz, S.; Arsenault, A. Dream Nanomachines. *Adv. Mater.* **2005**, *17*, 3011–3018.

15. DiLuzio, W. R.; Turner, L.; Mayer, M.; Garstecki, P.; Weibel, D. B.; Berg, H. C.; Whitesides, G. M. *Escherichia coli* Swim on the Right-Hand Side. *Nature* **2005**, *435*, 1271–1274.
16. Hong, Y.; Velegol, D.; Chaturvedi, N.; Sen, A. Biomimetic Behavior of Synthetic Particles: From Microscopic Randomness to Macroscopic Control. *Phys. Chem. Chem. Phys.* **2010**, *12*, 1423–1435.
17. Sengupta, S.; Ibele, M. E.; Sen, A. Fantastic Voyage: Designing Self-Powered Nanorobots. *Angew. Chem., Int. Ed.* **2012**, *51*, 8434–8445.
18. Mei, Y.; Huang, G.; Solovev, A. A.; Ureña, E. B.; Mönch, I.; Ding, F.; Reindl, T.; Fu, R. K. Y.; Chu, P. K.; Schmidt, O. G. Versatile Approach for Integrative and Functionalized Tubes by Strain Engineering of Nanomembranes on Polymers. *Adv. Mater.* **2008**, *20*, 4085–4090.
19. Solovev, A. A.; Mei, Y.; Bermudez Urena, E.; Huang, G.; Schmidt, O. G. Catalytic Microtubular Jet Engines Self-Propelled by Accumulated Gas Bubbles. *Small* **2009**, *5*, 1688–1692.
20. Paxton, W. F.; Kistler, K. C.; Olmeda, C. C.; Sen, A.; St. Angelo, S. K.; Cao, Y.; Mallouk, T. E.; Lammert, P. E.; Crespi, V. H. Catalytic Nanomotors: Autonomous Movement of Striped Nanorods. *J. Am. Chem. Soc.* **2004**, *126*, 13424–13431.
21. Wang, W.; Chiang, T.; Velegol, D.; Mallouk, T. E. Understanding the Efficiency of Autonomous Nano- and Microscale Motors. *J. Am. Chem. Soc.* **2013**, *135*, 10557–10565.
22. Wang, W.; Duan, W.; Ayusman, S.; Mallouk, T. E. Catalytically Powered Dynamic Assembly of Rod-Shaped Nanomotors and Passive Tracer Particles. *Proc. Natl. Acad. Sci. U.S.A.* **2013**, *110*, 17744–17749.
23. Petit, T.; Zhang, L.; Peyer, K. E.; Kratochvil, B. E.; Nelson, B. J. Selective Trapping and Manipulation of Microscale Objects Using Mobile Microvortices. *Nano Lett.* **2012**, *12*, 156–160.
24. Peyer, K. E.; Zhang, L.; Nelson, B. J. Bio-Inspired Magnetic Swimming Microrobots for Biomedical Applications. *Nanoscale* **2013**, *5*, 1259–1272.
25. Gao, W.; Feng, X.; Pei, A.; Kane, C. R.; Tam, R.; Hennessy, C.; Wang, J. Bioinspired Helical Microswimmers Based on Vascular Plants. *Nano Lett.* **2014**, *14*, 305–310.
26. Gao, W.; Pei, A.; Dong, R.; Wang, J. Catalytic Iridium-Based Janus Micromotors Powered by Ultralow Levels of Chemical Fuels. *J. Am. Chem. Soc.* **2014**, *136*, 2276–2279.
27. Gibbs, J. G.; Zhao, Y.-P. Autonomously Motile Catalytic Nanomotors by Bubble Propulsion. *Appl. Phys. Lett.* **2009**, *94*, 163104.
28. Wang, H.; Zhao, G.; Pumera, M. Beyond Platinum: Bubble-Propelled Micromotors Based on Ag and MnO_2 Catalysts. *J. Am. Chem. Soc.* **2014**, *136*, 2719–2722.
29. Soler, L.; Magdanz, V.; Fomin, V. M.; Sanchez, S.; Schmidt, O. G. Self-Propelled Micromotors for Cleaning Polluted Water. *ACS Nano* **2013**, *7*, 9611–9620.
30. Gao, W.; Uygun, A.; Wang, J. Hydrogen-Bubble-Propelled Zinc-Based Microengines in Strongly Acidic Media. *J. Am. Chem. Soc.* **2012**, *134*, 897–900.
31. Sanchez, S.; Solovev, A. A.; Mei, Y. F.; Schmidt, O. G. Dynamics of Biocatalytic Microengines Mediated by Variable Friction Control. *J. Am. Chem. Soc.* **2010**, *132*, 13144–13145.
32. Palacci, J.; Sacanna, S.; Vatchinsky, A.; Chaikin, P. M.; Pine, D. J. Photoactivated Colloidal Dockers for Cargo Transportation. *J. Am. Chem. Soc.* **2013**, *135*, 15978–159841.
33. Campuzano, S.; Orozco, J.; Kagan, D.; Guix, M.; Gao, W.; Sattayasamitsathit, S.; Claussen, J. C.; Merkoc, A.; Wang, J. Bacterial Isolation by Lectin-Modified Microengines. *Nano Lett.* **2012**, *12*, 396–401.
34. Wilson, D. A.; Nolte, R. J. M.; van Hest, J. C. M. Autonomous Movement of Platinum-Loaded Stomatocytes. *Nat. Chem.* **2012**, *4*, 268–274.
35. Loget, G.; Kuhn, A. Propulsion of Microobjects by Dynamic Bipolar Self-Regeneration. *J. Am. Chem. Soc.* **2010**, *132*, 15918–15919.
36. Loget, G.; Kuhn, A. Electric Field-Induced Chemical Locomotion of Conducting Objects. *Nat. Commun.* **2011**, *2*, 535.
37. Howse, J. R.; Jones, R. A.; Ryan, A. J.; Gough, T.; Vafabakhsh, R.; Golestanian, R. Self-Motile Colloidal Particles: From Directed Propulsion to Random Walk. *Phys. Rev. Lett.* **2007**, *99*, 048102.
38. Fisher, P.; Ghosh, A. Magnetically Actuated Propulsion at Low Reynolds Numbers: Towards Nanoscale Control. *Nanoscale* **2011**, *3*, 557–563.
39. Ghosh, A.; Fischer, P. Controlled Propulsion of Artificial Magnetic Nanostructured Propellers. *Nano Lett.* **2009**, *9*, 2243–2245.
40. Pumera, M. Electrochemically Powered Self-Propelled Electrophoretic Nanosubmarines. *Nanoscale* **2010**, *2*, 1643–1649.
41. Solovev, A. A.; Sanchez, S.; Pumera, M.; Mei, Y. F.; Schmidt, O. G. Magnetic Control of Tubular Catalytic Microbots for the Transport, Assembly, and Delivery of Micro-objects. *Adv. Funct. Mater.* **2010**, *20*, 2430–2435.
42. Gao, W.; Sattayasamitsathit, S.; Manesh, K. M.; Weihs, D.; Wang, J. Magnetically Powered Flexible Metal Nanowire Motors. *J. Am. Chem. Soc.* **2010**, *132*, 14403–14405.
43. Liu, Z.; Li, J.; Wang, J.; Huang, G.; Mei, Y. Small-Scale Heat Detection Using Catalytic Microengines Irradiated by Laser. *Nanoscale* **2013**, *5*, 1345–1352.
44. Jiang, H. R.; Yoshinaga, N.; Sano, M. Active Motion of a Janus Particle by Self-Thermophoresis in a Defocused Laser Beam. *Phys. Rev. Lett.* **2010**, *105*, 268302.
45. Balasubramanian, S.; Kagan, D.; Manesh, K. M.; Calvo-Marzal, P.; Flechsig, G.-U.; Wang, J. Thermal Modulation of Nanomotor Movement. *Small* **2009**, *5*, 1569–1574.
46. Sanchez, S.; Ananth, A. N.; Fomin, V. M.; Viehrig, M.; Schmidt, O. G. Superfast Motion of Catalytic Micromotors at Physiological Temperature. *J. Am. Chem. Soc.* **2011**, *133*, 14860–14863.
47. Magdanz, V.; Stoychev, G.; Ionov, L.; Sanchez, S.; Schmidt, O. G. Stimuli-Responsive Microjets with Reconfigurable Shape. *Angew. Chem., Int. Ed.* **2014**, *126*, 2711–2715.
48. Hong, Y.; Blackman, N.; Kopp, N.; Sen, A.; Velegol, D. Chemotaxis of Nonbiological Colloidal Rods. *Phys. Rev. Lett.* **2007**, *99*, 178103.
49. Wilson, D. A.; Nijs, B.; de Blaaderen, A.; van Nolte, R. J. M.; van Hest, J. C. M. Fuel Concentration Dependent Movement of Supramolecular Catalytic Nanomotors. *Nanoscale* **2013**, *5*, 1315–1318.
50. Yadav, V.; Zhang, H.; Pavlick, R.; Sen, A. Triggered "On/Off" Micropumps and Colloidal Photodiode. *J. Am. Chem. Soc.* **2012**, *134*, 15688–15691.
51. Solovev, A. A.; Smith, E. J.; Bufon, C. C. B.; Sanchez, S.; Schmidt, O. G. Light-Controlled Propulsion of Catalytic Microengines. *Angew. Chem., Int. Ed.* **2011**, *50*, 10875–10878.
52. Kolesnikova, T. A.; Kohler, D.; Skirtach, A. G.; Möhwald, H. Laser-Induced Cell Detachment, Patterning, and Regrowth on Gold Nanoparticle Functionalized Surfaces. *ACS Nano* **2012**, *6*, 9585–9595.
53. Wu, Z.; Wu, Y.; He, W.; Lin, X.; Sun, J.; He, Q. Self-Propelled Polymer-Based Multilayer Micromotors for Transportation and Drug Release. *Angew. Chem., Int. Ed.* **2013**, *52*, 7000–7003.
54. Jan, E.; Kotov, N. Successful Differentiation of Mouse Neural Stem Cells on Layer-by-Layer Assembled Single-Walled Carbon Nanotube Composite. *Nano Lett.* **2007**, *7*, 1123–1128.
55. Brown, K. R.; Natan, M. J. Hydroxylamine Seeding of Colloidal Au Nanoparticles in Solution and on Surfaces. *Langmuir* **1998**, *14*, 726–728.
56. Lee, J. H.; Engler, J. A.; Collawn, J. F.; Moore, A. Receptor Mediated Uptake of Peptides that Bind the Human Transferrin Receptor. *Eur. J. Biochem.* **2001**, *268*, 2004–2012.
57. Zhang, M.; Yu, R.; Chen, J.; Ma, Z.; Zhao, Y. Targeted Quantum Dots Fluorescence Probes Functionalized with Aptamer and Peptide for Transferrin Receptor on Tumor Cells. *Nanotechnology* **2012**, *23*, 485104.
58. Govorov, A. O.; Richardson, H. H. Generating Heat with Metal Nanoparticles. *Nano Today* **2007**, *2*, 30–34.
59. Buttinoni, I.; Volpe, G.; Kummel1, F.; Volpe, G.; Bechinger, C. Active Brownian Motion Tunable by Light. *J. Phys.: Condens. Matter* **2012**, *24*, 284129.
60. Merabia, S.; Shenogin, S.; Joly, L.; Keblinski, P.; Barrat, J. L. Heat Transfer from Nanoparticles: A Corresponding State Analysis. *Proc. Natl. Acad. Sci. U.S.A.* **2009**, *106*, 15113–15118.

61. Wu, Y.; Wu, Z.; Lin, X.; He, Q.; Li, J. Autonomous Movement of Controllable Assembled Janus Capsule Motors. *ACS Nano* **2012**, *6*, 10910–10916.
62. Li, D.; He, Q.; Cui, Y.; Li, J. Fabrication of pH-Responsive Nanocomposites of Gold Nanoparticles/Poly(4-vinylpyridine). *Chem. Mater.* **2007**, *19*, 412–417.
63. Fujimoto, H.; Oku, Y.; Ogihara, T.; Takuda, H. Hydrodynamics and Boiling Phenomena of Water Droplets Impinging on Hot Solid. *Int. J. Multiphase Flow* **2010**, *36*, 620–642.